Journal of Nuclear Materials 405 (2010) 118–125

Contents lists available at ScienceDirect

Journal of Nuclear Materials

journal homepage: www.elsevier.com/locate/jnucmat

Measurement of radiation-enhanced diffusion of La in single crystal thin film CeO_2

Harrison K. Pappas, Brent J. Heuser *, Melissa M. Strehle

Department of Nuclear, Radiological, and Plasma Engineering, University of Illinois at Urbana-Champaign, Urbana, IL 61801, United States

ARTICLE INFO

Article history:
Received 4 June 2010
Accepted 26 July 2010

ABSTRACT

The diffusion of La, a trivalent cation dopant, actinide surrogate, and high-yield fission product, in CeO_2, a UO_2 nuclear fuel surrogate, during 1.8 MeV Kr^+ ion bombardment over a temperature range from 673 K to 1206 K has been measured with secondary ion mass spectroscopy. The diffusivity under these irradiation conditions has been analyzed with a model based on a combination of sink-limited and recombination-limited kinetics. This analysis yielded a cation vacancy migration energy of $E_m^v \sim 0.4$ eV below ~800 K, were recombination-limited kinetics dominated the behavior. The thermal diffusivity of La in the same system was measured over a range of 873–1073 K and was characterized by an activation enthalpy of $E_a = E_f^v + E_m^v \sim 1.4$ eV. The measurement of both the migration enthalpy and total activation enthalpy separately allows the vacancy formation enthalpy on the cation sublattice to be determined; $E_f^v \sim 1$ eV. The mixing parameter under energetic heavy-ion bombardment at room temperature was measured as well and found to be $\sim 4 \times 10^{-5}$ nm^5/eV.

1. Introduction

Enhanced diffusion under energetic heavy-ion bombardment occurs because point defect populations are elevated over thermal equilibrium by displacement cascade damage [1,2]. Fission fragments in UO_2 represent such a bombardment scenario. The transport of all chemical species, whether regular lattice atoms or impurities, in nuclear fuel results in dimensional instability, grain morphological changes, open pore volume/bubble formation, and precipitation [3]. The effect of radiation-enhanced diffusion (RED) on impurity transport is of special interest in a closed nuclear fuel cycle, where transuranic actinides, the most long-lived of all neutron irradiation by-products in UO_2, are removed from spent fuel and incorporated into fresh fuel for transmutation [4]. Recycling Pu in a closed fuel cycle leads to the MOX fuel form, which allows the energy content of fissile Pu-239 and Pu-241 to be recovered in LWRs. Transmutation of the recycled minor actinides (Np, Am, and Cm, for example) in either LWRs or fast reactors can potentially reduce the nuclear fuel waste storage requirements by hundreds of thousands years. However, little is known regarding the behavior of minor actinides in the UO_2 fuel matrix during operation [5]. In particular, precipitation can alter the mechanical and thermal response of the fuel form. Here we address the underlying process, the accelerated or enhanced transport of impurities in the high-temperature, energetic heavy ion irradiation environment of nuclear fuel.

We have used secondary ion mass spectroscopy (SIMS) to measure the La depth profiles in an epitaxial single crystal CeO_2 thin film. The CeO_2 system is often used as a UO_2 fuel surrogate because Ce is typically found in the +4 valence state with an ionic radius similar to uranium. As a consequently, the crystal structure of CeO_2 and UO_2 are both Fm-3 m (the fluorite structure) with nearly identical lattice parameters (0.5411 versus 0.5464 nm, respectively). Lanthanum is most commonly found in the +3 valence state and is therefore an attractive surrogate for Am, which is difficult to oxidize beyond +3 and does not readily form a dioxide compound without the aid of oxidizing agents. In addition, La-139 is the terminal (stable) isotope of the $A = 139$ fission product decay sequence and is produced with a yield of 6.41% during U-235 thermal fission.

The experimental procedures are presented in the next section. This will include sample preparation and characterization, energetic heavy-ion bombardment conditions, and SIMS measurement characteristics. SIMS measurements of La depth profiles will be presented in the results section. This presentation will include the conversion of La depth profile width to diffusivity. A kinetic rate model originally published by Dienes and Damask [2] will be used to analyze the measured diffusivities under irradiation. A shift of diffusivity from recombination-limited to sink-limited kinetics and ultimately to thermal vacancy self-diffusion (VSD) as temperature increases under irradiation is understood within this model. The cation vacancy migration and formation enthalpies determined from the model fit are discussed within the context of cation and anion transport in ionic compounds such as CeO_2.

* Corresponding author. Tel.: +1 217 333 9610; fax: +1 217 333 2906.
E-mail address: bheuser@illinois.edu (B.J. Heuser).

0022-3115/$ - see front matter © 2010 Elsevier B.V. All rights reserved.
doi:10.1016/j.jnucmat.2010.07.042

2. Experimental

A 37.0-nm thick single crystal CeO_2 film on epi-polished r-plane [1 $\bar{1}$ 0 2] sapphire (0.25° miscut angle, 1 mm thick) was grown at 973 K by ozone-assisted molecular beam epitaxy with a monolayer of La at the film half thickness. The overall substrate dimension was a 15×15 mm^2. Twelve individual 3×3 mm^2 samples were cut from this substrate after growth. The total film thickness was obtained from thickness oscillations observed in an X-ray reflectivity measurement (not shown). In addition, measurements of SIMS craters from three different samples using a Sloan Dektak-3 ST profilometer yielded results consistent with a 37 nm film thickness. *In situ* RHEED analysis during the film deposition indicated good three-dimensional crystalline growth [6]. The film was grown under an ozone pressure of approximately 10^{-3} Pa at a growth rate of approximately ~0.01 nm per second. The amount of La deposited (1 monolayer) is an estimate based on the known evaporation flux for the La source [7].

X-ray diffraction (XRD) analysis was performed with a Philips X'Pert diffractometer with a Cu Kα source ($\lambda = 0.15406$ nm). Specular Ω-2θ and in-plane φ XRD scans of representative samples are shown in Figs. 1 and 2, respectively. The specular scans are along the [0 0 *l*] film normal direction. The specular scan of the un-irradiated reference sample indicates a [0 0 1] preferred growth direction that does not change significantly with high-temperature heavy-ion bombardment. A portion of the as-grown, un-irradiated film exhibits a [1 1 1] preferred growth direction, as indicated by the presence of a small peak corresponding to the (1 1 1) reflection. The area under the (1 1 1) peak is approximately 20% of the (0 0 2) peak for the as-grown measurement. This corresponds to ~7% of the total film volume since the (1 1 1):(0 0 2) structure factor ratio is 1:0.36. We believe this volume fraction represents an upper limit since other areas of the sample (the 295 K/1.25×10^{19} and 773 K/1.0×10^{20} m^{-2} sample areas, for example) have significantly lower (1 1 1) peak intensity. The (2 2 0) φ scans shown in Fig. 2 demonstrates that the as-grown un-irradiated film consisted of a single-domain. The fourfold symmetry observed from the (2 2 0) in-plane reflection is that expected of single crystal CeO_2 on r-plane sapphire, as observed by others [8,9]. Here it is important to draw a distinction between a highly textured polycrystalline film and a true single crystal film. The former would not exhibit sharp peaks in an in-plane φ scan, but instead would either be featureless or exhibit broad weak peaks. Fig. 2 also demonstrates that high-temperature, heavy-ion bombardment does not eliminate the single-domain structure.

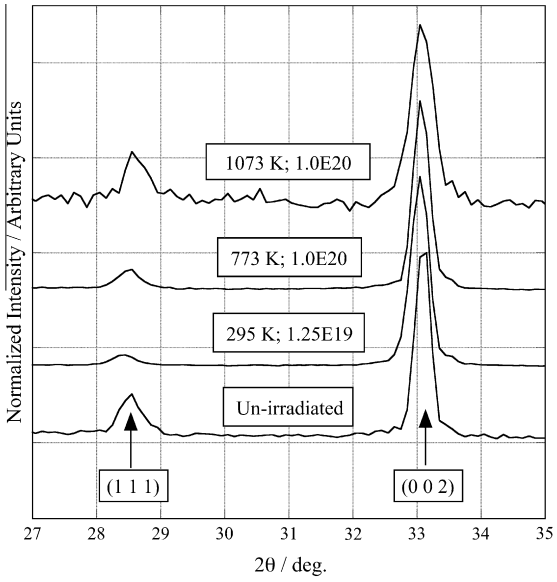

Fig. 1. Normalized specular X-ray diffraction scans along the [0 0 *l*] film normal direction showing the angular range containing the (1 1 1) and (0 0 2) reflections; other than the (0 0 4) second order peak, no other CeO_2 reflections were observed in any specular scan. The sample treatment conditions (irradiation temperature followed by fluence in units of ions/m^2) are indicated for each measurement. Each scan is normalized to the peak intensity from the (0 0 2) reflection. The intensity from the (1 1 1) reflection is weak, indicating preferred growth along the (0 0 2) direction (see text). The scans have been shifted vertically for clarity.

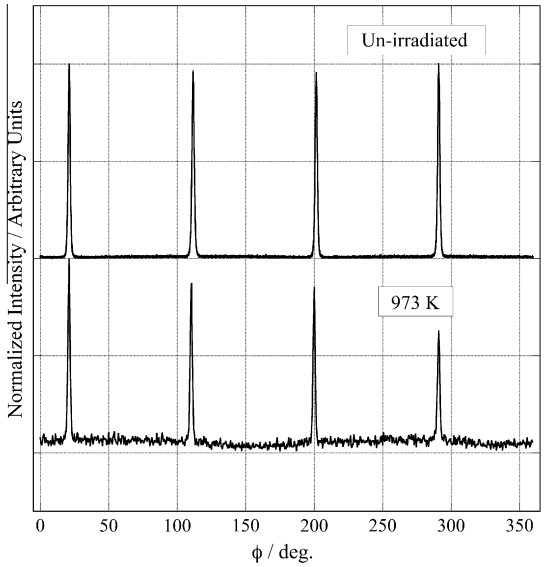

Fig. 2. Normalized X-ray diffraction φ scans of the (2 2 0) in-plane reflection from as-grown, un-irradiated (upper scan) and at-temperature irradiated (lower scan) single crystal CeO_2 samples. The irradiated sample was bombarded to a fluence of 1×10^{20} ions/m^2 at 973 K. The fourfold in-plane symmetry demonstrates that the as-grown film consisted of a single lattice domain and that high-temperature irradiation did not significantly alter this structure. The two scans have been shifted vertically for clarity.

The conclusion that the ceria film investigated here is single crystal rather than a textured polycrystal film is important since it allows us to attribute the measured La diffusivities to a cation diffusion process that is not influenced by large angle grain boundaries that comprise polycrystalline microstructures. Furthermore, the effect of high-temperature heavy-ion bombardment on the single crystal nature of the film is not significant, except for mosaic broadening discussed below. We are therefore confident that the observed shift in point defect transport behavior from recombination-limited to sink-limited kinetics as the irradiation temperature increases is not due to the creation of grain boundaries.

A rocking curve scan of the reference un-irradiated film is shown in Fig. 3, as are post-irradiated scans of two samples bombarded to a dose or fluence of 10^{20} ions/m^2. The rocking curve scan of the reference film is characterized by a narrow component ($\sigma \sim 0.02°$) and a broad component ($\sigma \sim 0.4°$), consistent with a portion of the film commensurate or in registry with the sapphire substrate and a portion of the film not in registry, respectively. Similar rocking curves have been observed from epitaxial (0 0 1) CeO_2 on r-plane sapphire and interpreted as nucleation along step edges (narrow mosaic) versus nucleation away from step edges (broad mosaic) [8]. We note the presence of a ~0.1° offset between the narrow and the broad components in the rocking curves. This offset is a consequence of portion of the film volume (the commensurate portion) following the single crystal sapphire template during growth, while the remaining incommensurate volume followed the free surface. The lattice mosaic is broadened significantly by heavy-ion bombardment above ~1000 K, as is evidently in the

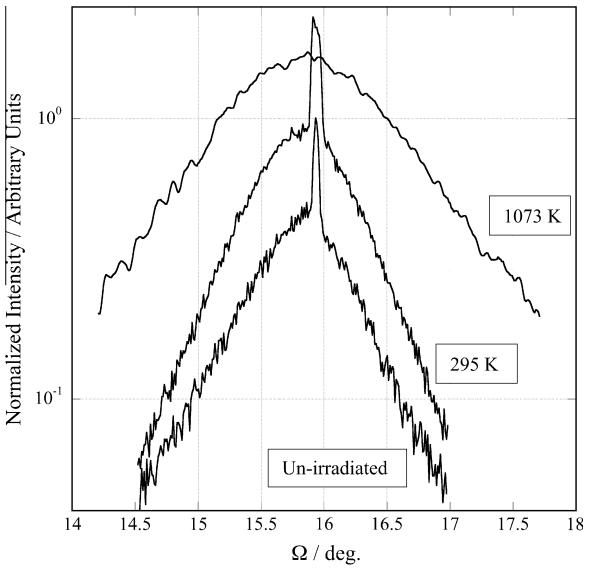

Fig. 3. X-ray diffraction rocking curve scans across the (0 0 2) reflection of un-irradiated and at-temperature irradiated single crystal CeO_2. The two irradiated samples were bombarded to a fluence of 1×10^{20} ions/m^2 at the temperatures indicated. The un-irradiated and $T = 295$ K irradiated sample are characterized by a narrow mosaic component and a broad mosaic component. The narrow mosaic component is eliminated by high-temperature heavy-ion bombardment. The scans have been shifted vertically for clarity.

1073 K data in Fig. 3. This broadening is due to dislocation generation associated with radiation damage.

A slightly compressive out-of-plane strain ($\varepsilon_z = -5.5 \times 10^{-4}$) was determined from the (0 0 2) peak position in the specular scan of the un-irradiated CeO_2 film in Fig. 1. Lattice strain is sensitive to oxygen stoichiometry in ceria because oxygen vacancies create trivalent cerium ions via the $2Ce'_{Ce} = V_O^{\cdot\cdot}$ neutrality condition (using Kröger-Vink notation [10]) and Ce^{+3} has a larger ionic radius compared to Ce^{+4}. Thus, tensile strain is observed for non-stoichiometric CeO_{2-x} that varies linearly with x [10]. We have measured a slightly compressive strain, which cannot be explained by hyper-stoichiometric ceria formation (in other words, CeO_{2+x}) since this compound is not known to occur. CeO_{2+x} would require a Ce^{+5} valence state or the formation of Ce^{+4} interstitials, both of which are energetically unfavorable. We therefore attribute the compressive out-of-plane strain to the Poisson response of a tensile in-plane strain of similar magnitude. Generally, strains of order $\sim|10^{-4}|$ in ceria are equivalent to stoichiometric $CeO_{2.00}$ [10].

Lanthanum depth profiles were measured with a Physical Electronics PHI Trift III SIMS at the University of Illinois. This instrument runs in time-of-flight mode and has excellent mass resolution over a range extending to 10,000 u. An O_2 beam was used for the sputter erosion to enhance the sensitivity to low electronegative metal species, while a Au ion analysis beam was used for data collection. These two ion beams were cycled to produce the measured depth profiles. The O_2 beam energy and incident angle used for sputtering were 2 keV and 45°, respectively. The samples were biased to +2 kV to enhance the sensitivity to positive secondary ions. Sputter erosion was performed over a 400×400 μm^2 area and the 50×50 μm^2 Au analysis beam was centered within the sputter crater. Some samples were coated with a ~5 nm layer of Au to eliminate surface charge buildup during sputter erosion and mass analysis. Ion beam induced mixing occurs with SIMS analysis since the depth profile measurement requires sputter erosion. For smooth samples with well defined interfaces or buried monolayers, this mixing is the limiting contribution of the depth resolution of SIMS profiles. We find that the depth resolution is characterized by a Gaussian standard deviation of $\sigma \sim 2.6$ nm. In our case, however, the broadening of the La layer via thermal diffusion during growth of the second half of the CeO_2 film at 973 K was a contributing factor to the measured depth resolution.

Energetic heavy-ion bombardment was performed with 1.8 MeV Kr^+ ions using a High Voltage Engineering Van de Graaff accelerator at the University of Illinois. The estimated implantation depth of Kr^+ into sapphire at this energy is ~650 nm, with negligible implantation into the CeO_2 film [11]. Two sets of irradiation experiments were performed; a set at room temperature where the fluence Φ was varied from zero to 2×10^{20} ions/m^2 and a set at constant fluence ($\Phi = 1 \times 10^{20}$ ions/m^2) where the temperature was varied from 673 to 1206 K. Individual samples were mounted on a resistive heater for irradiation at elevated temperature (referred to as at-temperature irradiation below) with a small K-type thermocouple temperature sensor attached directly to the film surface at a corner location with Ag paste. The entire sample, except for one corner, was bathed with a 3×3 mm^2 ion beam. The beam current was measured periodically during irradiation by the insertion of a Faraday cup. Stable beam currents of 100 nA were typical—a fluence of 1×10^{20} ions/m^2 required an irradiation time of 20 min at this current. Approximately 25% of each at-temperature irradiated sample, including the thermocouple sensor and Ag paste, was blocked from the ion beam and analyzed for the thermal-only (same time–temperature history without ion bombardment) diffusivity measurement. The room temperature set of irradiations was performed to determine the mixing parameter. These samples were mounted to a heat sink with Ag paste during irradiation. Neither Ag nor Au was observed in any of the SIMS profiles, indicating that these elements did not diffuse into or otherwise contaminate the film during irradiation or SIMS analysis. Implanted Kr was not observed either, although the detection of inert species is difficulty with SIMS. All irradiations were performed under a vacuum of 10^{-4} Pa or better.

The conversion from energetic heavy-ion bombardment fluence to fuel burnup in terms of fissions per initial fissile metal atom (FIMA) is useful to consider. Typical burnup values in LWRs are ~0.04 FIMA, with so-called deep burn operation approaching 0.1 FIMA. The burnup corresponding to the at-temperature irradiation fluence of 1×10^{20} ions/m^2 used here is ~0.02 FIMA and is therefore representative of realistic fuel burnup levels. This conversion assumes 4% enrichment, that each U-235 fission produces two 100 MeV fission fragments with $A \sim 120$ u, that these fission products produce a total of 10^5 Frenkel pairs (one Frenkel pair corresponds to one displaced atom) in the UO_2 fuel matrix [11], that the nuclear differential energy deposition for 1.8 MeV Kr^+ ions in CeO_2 of 1150 eV/nm/ion [11], and that 25 eV is required to produce a Frenkel pair. Under these assumptions 1 FIMA corresponds to ~1300 displacements per atom (dpa) in UO_2. Likewise, a 1.8 MeV-Kr^+ fluence of 1×10^{20} ions/m^2 corresponds to ~25 dpa in CeO_2. The conversion from fluence to FIMA is then given by the dpa ratio $25/1300 \sim 0.02$ FIMA.

3. Results

Lanthanum depth profiles from the room temperature set of irradiations measured with SIMS are shown in Fig. 4. Each depth profile has been fit with a Gaussian distribution and the standard deviations σ characterizing these fits are listed in Table 1. The La yield has been normalized in all depth profiles presented here by setting the area under each curve to one. This normalization assumes the total amount of La in each sample has remained the same. This is a reasonable assumption given all samples originated from the same deposition and the loss of La from the samples is not

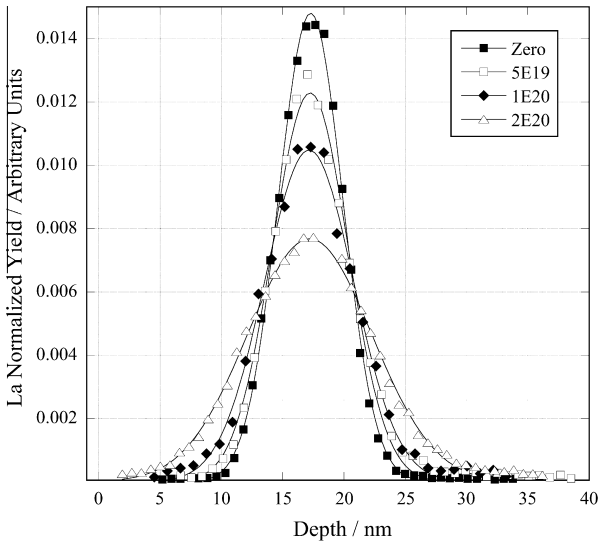

Fig. 4. Normalized La depth profiles for single crystal CeO_2 irradiated at 295 K to fluences in units of ions/m^2 as indicated. The free surface corresponds to zero depth, while the film substrate interface is at a depth of 37.0 nm. The solid lines are drawn best-fits to a Gaussian distribution. The standard deviations from these fits are listed in Table 1.

Table 1
Irradiation conditions, measured La profile standard deviations, and measured diffusivities.

T (°K)	Φ (1/nm^2)	σ (nm)	D ($\times 10^{-20}$ m^2/s)
295	0	2.62 ± 0.02	–
295	50	3.08 ± 0.04	0.11 ± 0.01
295	100	3.61 ± 0.07	0.26 ± 0.03
295	200	5.09 ± 0.06	0.79 ± 0.05
873	0	2.89 ± 0.02	0.062 ± 0.007
873	0	2.90 ± 0.02	0.064 ± 0.007
973	0	3.85 ± 0.05	0.33 ± 0.02
1073	0	8.16 ± 0.15	2.5 ± 0.2
673	100	5.25 ± 0.09	0.61 ± 0.05
773	100	6.44 ± 0.28	1.2 ± 0.2
873	100	7.08 ± 0.20	1.6 ± 0.1
973	100	7.26 ± 0.17	1.7 ± 0.1
973	100	7.68 ± 0.11	1.9 ± 0.1
1073	100	9.34 ± 0.13	3.1 ± 0.2
1073	100	9.47 ± 0.11	3.2 ± 0.2
1073	100	10.05 ± 0.14	3.7 ± 0.2
1206	100	14.6 ± 0.4	8.3 ± 0.6

expected to occur, even under heavy-ion bombardment. The depth axis associated with each SIMS measurement was placed on absolute scale by setting the point at which the CeO (the strongest signal from the CeO_2 film) and Al (the strongest signal from the Al_2O_3 substrate) mass signals cross to a depth of 37.0 nm.

The variable-fluence irradiations at room temperature were performed to measure the mixing parameter ξ in CeO_2 using the La as a tracer. The mixing parameter is defined as:

$$\xi = Dt/\Phi F_D, \tag{1}$$

where D is the diffusivity, t is the irradiation time, Φ is the fluence, and F_D = 1150 eV/nm/ion is the nuclear differential energy deposition for 1.8 MeV Kr^+ ions in CeO_2 [11]. The product Dt is given by the relation:

$$2Dt = (\sigma_{irr})^2 - (\sigma_{ref})^2, \tag{2}$$

where σ_{irr} and σ_{ref} are the Gaussian standard deviations for the irradiated and zero-fluence reference (σ_{ref} = 2.62 nm) La distributions measured with SIMS, respectively. This equation assumes a one-dimension diffusion or mixing geometry, as is the case with the semi-infinite buried La layer studied here.

The mixing parameter defined by Eq. (1) is a constant of proportionality that equates the total nuclear differential energy deposition (the product ΦF_D) to the total mean square displacement (the product Dt) induced by displacement cascade damage. The room-temperature mixing parameter characterizes the diffusivity associated with displacement cascades since long-range transport associated with elevated temperature does not occur. The analysis associated with Eq. (1) is shown in Fig. 5 and yields ξ = 3.6 (0.5) $\times 10^{-5}$ nm^5/eV, a low value indicative of ballistic mixing without significant thermal-spike mixing. Thermal-spike mixing refers to local atomic transport that may occur during the dissipation of thermal energy (which locally heats the crystal lattice) immediately after the collisional (ballistic) phase of a displacement cascade [12]. The low mixing parameter in CeO_2 is likely due to two effects. First, CeO_2 has a high melting temperature (2673 K) and this will reduce atomic transport during the thermal-spike phase because of larger cohesive lattice energy. The opposite is true of low melting temperature metals such as Au ($\xi \sim 120 \times 10^{-5}$ nm^5/eV [12]) and Ag ($\xi \sim 75 \times 10^{-5}$ nm^5/eV [12]), for example. In addition, the thermal diffusivity of the La in CeO_2 is low, as presented below, and this will reduce the marker transport during the thermal-spike phase of the displacement cascades. We know of one other example of a measured mixing parameter at room temperature in a ceramic compound, $\xi \sim 1$–5×10^{-5} nm^5/eV for MgO [13].

The La depth profiles for the at-temperature irradiations are shown in Fig. 6 with the Gaussian best-fits. We show only the leading edge of the depth profiles to better highlight the changes induced by irradiation. The absolute depth scale axis was set using the same procedure as Fig. 4. The 1206 K depth profile is shown on an expanded scale in Fig. 6 inset. The 1206 K data normalized the same way as the other SIMS profiles in Fig. 6 would appear flat on the scale of the primary figure since significant broadening occurred at this temperature. In fact, the broadening induced at 1206 K during irradiation is approaching the limit of sensitivity of our procedure since a measurable concentration gradient is required to determine the diffusivity. The standard deviations, σ, from all the SIMS measurements, at-temperature and variable-fluence,

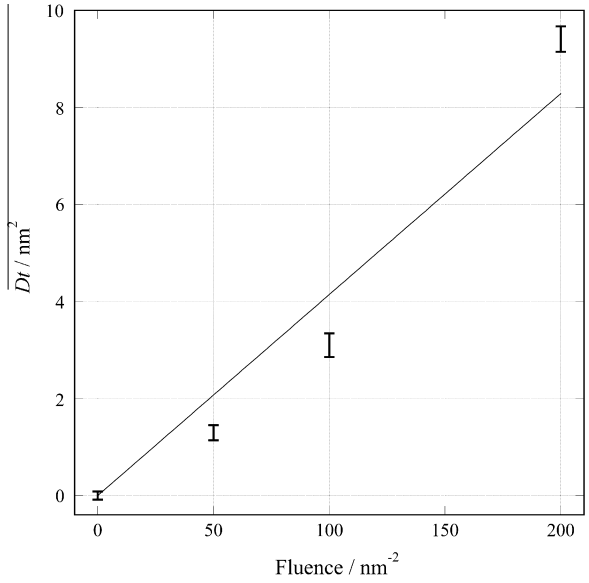

Fig. 5. Product Dt (the total mean squared displacement in one-dimensional diffusion) versus fluence (in units of ions/nm^2) for heavy-ion bombardment at 295 K. The best-fit line, which is forced through the origin (zero displacement at zero fluence), is proporational to the mixing parameter as discussed in the text.

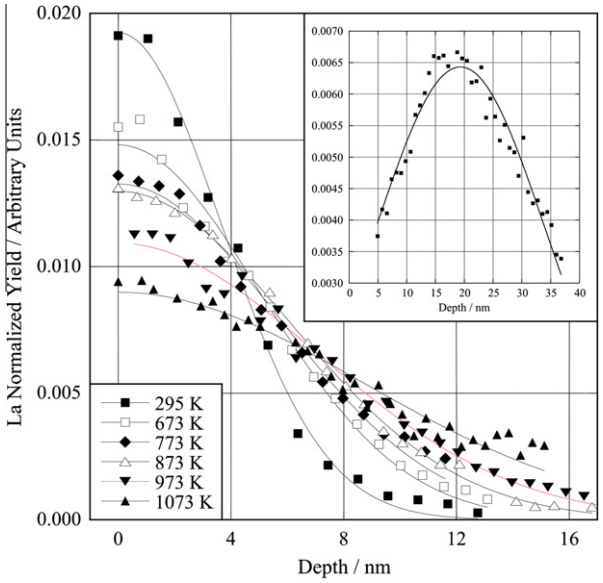

Fig. 6. Normalized La depth profiles for single crystal CeO_2 irradiated at a fluence of 10^{20} ions/m^2 at the temperatures indicated. The depth scale is inverted so that zero depth corresponds to the film half-width and the center of the La profiles. The solid lines are best-fits of a Gaussian distribution to the leading edge of the La depth profiles. The inset shows the best-fit of the 1206 K depth profile. The standard deviations obtained from these best-fits are listed in Table 1.

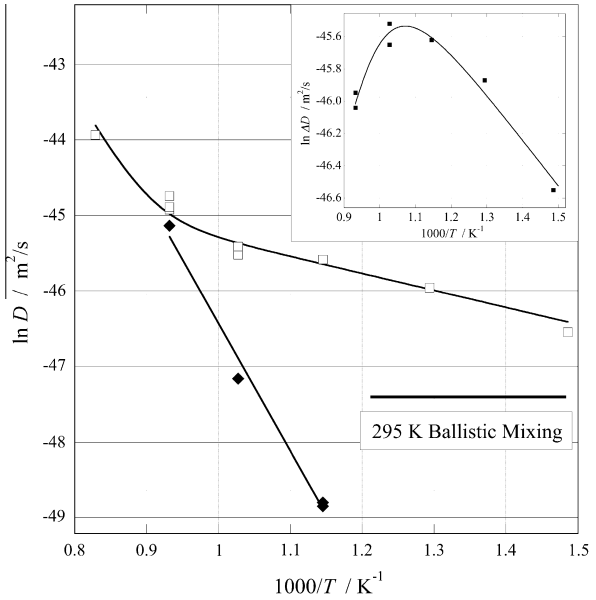

Fig. 7. Arrhenius plot of the measured diffusivities at elevated temperature during heavy-ion bombardment (D', open boxes) and at elevated temperature in the absence of heavy-ion bombardment (D_T, solid diamonds). More than one measurement was performed at a given temperature in a few cases and these are plotted as individual data points. The diffusivity associated with ballistic mixing at 295 K ($\Phi = 10^{20}$ ions/m^2) is shown as a thick horizontal line. The solid line through the measured diffusivities under heavy-ion bombardment is a best-fit of a diffusion model based on a combination of sink-limited and recombination-limited kinetics, as discussed in the text. The measured data in the absence of heavy-ion bombardment is fit with an Arrhenius law for regular lattice diffusion. The errors associated with each diffusivity measurement are comparable to the size of the plotting symbols and not shown. Inset: Arrhenius plot of the ΔD showing the high-temperature reduction in diffusivity expected without the thermal VSD contribution. See text for further discussion.

are listed in Table 1. In addition, three thermal-only measurements at 873, 973, and 1073 K are listed on Table 1. These were the only three thermal-only samples that exhibited a measurable broadening. The thermal-only profiles at 673 and 773 K were not broadened above the $\sigma = 2.62$ nm resolution measured for the zero-fluence reference sample. In other words, the thermal diffusivity was too low to resolve at these temperatures. Unfortunately, we could not obtain meaningful SIMS data from the 1206 K thermal-only sample area despite several attempts (which consumed the entire unirradiated area). We suspect the Au coating was not adequate in this region of the sample to prevent charge buildup. Charge buildup strongly influences SIMS analysis by unpredictably deflecting the sputter beam and/or analytical beam from the common measurement area. Multiple SIMS measurements were performed on a few samples and the standard deviations of these profiles are listed in Table 1.

Each at-temperature irradiated σ value in Table 1 can be converted to a diffusivity D using Eq. (2) with $\sigma_{ref} = 3.61$ nm (the $T = 295$ K $\Phi = 1 \times 10^{20}$ m^{-2} standard deviation) and $t = 1200$ s (the time required to obtain a dose of 1×10^{20} m^{-2}). The use of this reference value subtracts the apparent diffusivity due to ballistic mixing at room temperature and as well as the instrumental resolution associated with SIMS analysis. The zero-fluence σ values in Table 1 can be converted to thermal-only diffusivities D_T using Eq. (2), but with $\sigma_{ref} = 2.62$ nm (the $T = 295$ K zero fluence standard deviation) and $t = 1200$ s (the time at elevated temperature). The use of this reference value subtracts the instrumental resolution associated with SIMS analysis. The uncertainties in all diffusion coefficients listed in Table 1 include the quoted error in σ as well as a 5% assumed error in the irradiation time to account for slight variations in irradiation beam current. An Arrhenius plot ($\log D$ versus $1000/T$) of the measured diffusivity is shown in Fig. 7. The thermal-only diffusivity has been fit with an Arrhenius response expected for VSD, $D_T = D_o \exp(-E_a/kT)$, where D_o is the diffusion constant and E_a is the activation enthalpy. These constants are listed in Table 2, together with the constants determined from the application of a model based on a set of kinetic rate equations presented in the next section.

Table 2
Fitting constants for at-temperature irradiated and thermal-only diffusion of La in CeO_2.

Type	T (K)	D_o (m^2/s)	E_a (eV)
D'	>1073	7.9×10^{-14}	1.42 ± 0.13
D'	673–873	–	0.19 ± 0.03
D_T	873–1073	1.5×10^{-13}	1.46 ± 0.11

It was stated above that thermal diffusion of the La monolayer during film growth was a contributing factor to the depth resolution associated with SIMS analysis. With the thermal diffusivity now in hand we can estimate this broadening directly assuming a film growth rate of 0.01 nm/s; $\sigma \sim [(37\,\text{nm}/0.01)\, D_T(973\,\text{K})]^{1/2} \sim 3.5$ nm. This estimate has perhaps a 50% uncertainty since the film growth rate and temperature are not precisely known.

4. Analysis

Point defect populations are elevated above thermal equilibrium during heavy-ion bombardment. The enhanced point defect population under irradiation is governed by the following set of kinetic rate equations [2]:

$$dv/dt = K - K_v v - \nu_i(v + v_o)i \tag{3a}$$

$$di/dt = K - K_i i - \nu_i(v + v_o)i, \tag{3b}$$

where v and i are the enhanced vacancy and interstitial atomic fractions during irradiation, respectively, v_o is the vacancy fraction

under thermal equilibrium, K is the production rate of Frenkel pairs due to heavy-ion bombardment, K_v and K_i are the removal rates of vacancies and interstitials at unsaturable sinks, respectively, and ν_i is the interstitial jump frequency. The last term on the right of Eq. (3) represents the removal of point defects due to recombination and is assumed to be dictated by interstitial transport. This is justified since the migration enthalpy of interstitials E_m^i is typically much smaller than that of vacancies and jump frequencies vary exponentially with E_m. Additionally, Eq. (3) ignores the interstitial atomic fraction associated with thermal equilibrium. This is justified as well since the formation enthalpy of interstitials E_f^i is much larger than that of vacancies and point defect concentrations vary exponentially with the E_f.

The product of the vacancy atomic fraction at thermal equilibrium v_o and the vacancy jump frequency ν_v is required to place the total diffusion coefficient during irradiation in final form. For completeness we give the product $i_o\nu_i$ as well. These are given by standard statistical thermodynamics as:

$$v_o\nu_v = A_v\nu\exp[(S_f^v + S_m^v)/k]\exp[-(E_f^v + E_m^v)/kT] \tag{4a}$$

$$i_o\nu_i = A_i\nu\exp[(S_f^i + S_m^i)/k]\exp[-(E_f^i + E_m^i)/kT] \tag{4b}$$

where ν is the characteristic lattice vibration frequency ($\nu \sim 10^{13}$ 1/s), A is a constant which includes a geometric factor, S is the entropy, and E is the enthalpy. The subscripts m and f denote migration and formation contributions, respectively, to the entropy and enthalpy.

Point defect diffusion to sinks and subsequent removal is accounted for in the rate equations. Point defect sinks include dislocations, free surfaces and buried interfaces, grain boundaries, voids, and internal surfaces associated with second phase particles. Of these, only dislocations are expected to influence point defect transport in our single phase, single crystal matrix. The free surface and CeO_2–Al_2O_3 interface are not expected to influence the diffusivity in the sink-limited kinetic regime. The time for La to reach either interface at 1000 K (the upper temperature limit of sink-limited kinetics) can be estimated with Eq. (2); $t \sim (37\text{ nm}/2)^2/2D' \sim 10^4$ s. This time is significantly longer than the irradiation time (1200 s). The point defect removal rates at dislocations are given by Dienes and Damask [2]:

$$K_v = \alpha\nu_v\lambda^2 \tag{5a}$$

$$K_i = \alpha\nu_i\lambda^2 \tag{5b}$$

where ν_v and ν_i are migration frequencies for vacancies and interstitials, respectively, λ is the jump distance and α is a constant of proportionality, which for dislocation defects, is given by Dienes and Damask [2]:

$$\alpha = \frac{2\pi N}{\ln(\frac{r_1}{r_o})} \approx N \tag{6}$$

where N is the dislocation density (in units of inverse area), $r_1 = \frac{1}{\sqrt{\pi N}}$ is the average dislocation separation and r_o is the effective radius of the dislocation (generally equated with the dislocation core width $\sim 10^{-1}$ nm). We have not attempted to measure N, which is expected to increase with heavy ion fluence. However, as discussed below, the enthalpies determined by the fit of the kinetic model are insensitive to α.

We are interested in the steady-state solutions to Eq. (3) for v and i, the enhanced vacancy and interstitial atomic fractions during irradiation, which are given by Dienes and Damask [2]:

$$v = -\frac{1}{2}(\alpha\lambda^2 + \nu_o) + \frac{1}{2}\left[(\alpha\lambda^2 + \nu_o)^2 + \frac{4K}{\nu_v}\right]^{1/2} \tag{7a}$$

$$i = \frac{1}{2\nu_i}\{-(\alpha\nu_v\lambda^2 + \nu_v\nu_o) + [(\alpha\nu_v\lambda^2 + \nu_v\nu_o)^2) + 4K\nu_v]^{1/2}\} \tag{7b}$$

Notice $i\nu_i = v\nu_v$ from Eq. (7). The enhanced diffusivities *during irradiation* from vacancy self-diffusion and interstitial diffusion are given by:

$$D'_v = v\nu_v\lambda^2 \tag{8a}$$

$$D'_i = i\nu_i\lambda^2 \tag{8b}$$

where v and i represent the enhanced atomic fractions given by Eq. (7). We can now write the total diffusion coefficient as:

$$\begin{aligned} D' &= D_T + D'_i + D'_v = \nu_o\nu_v\lambda^2 + v\nu_v\lambda^2 + i\nu_i\lambda^2 \\ &= \nu_o\nu_v\lambda^2 + 2v\nu_v\lambda^2 = \nu_v\lambda^2(\nu_o + 2v) \end{aligned} \tag{9}$$

where D_T is the thermal diffusion coefficient in the absence of heavy-ion bombardment and is governed by the vacancies under thermal equilibrium (thermal VSD). The relation $i\nu_i = v\nu_v$ has been used in the intermediate step of Eq. (9). The best-fit of Eq. (9) to the at-temperature irradiated diffusivity is shown in Fig. 7 and discussed below.

The assumption that $dv/dt = di/dt = 0$ can be justified by considering the time to reach a steady state point defect population under irradiation. Following Dienes and Damask [2], this time is estimated by $\tau \sim (k\nu_v)^{-1/2} \sim 10^{-1}$ s. This time is extremely short compared to the total irradiation time (1200 s), primarily because of the large defect production rate ($K \sim 0.02\text{ s}^{-1}$) for heavy-ion bombardment.

5. Discussion

The diffusivity under heavy-ion bombardment can be separated into three temperature ranges. At low temperature ($T < 800$ K for the present work), where the contribution of the thermal vacancy population to the observed diffusivity is small and the loss of point defects to sinks is low because of slow diffusion, the diffusivity is given approximately by:

$$\begin{aligned} D' &= \nu_v\lambda^2(\nu_o + 2v) \simeq 2v\nu_v\lambda^2 \\ &\simeq 2\lambda^2\sqrt{vA_vK}\exp(S_m^v/2k)\exp(-E_m^v/2kT) \end{aligned} \tag{10}$$

An Arrhenius behavior is expected with an activation enthalpy given by $E_a = E_m^v/2$. As discussed by Dienes and Damask [2], this temperature regime is characterized by recombination-limited kinetics. At high temperature ($T > 1100$ K for the present work), where thermal vacancy equilibrium begins to dominate the vacancy population, the diffusivity is approximated by:

$$D' \simeq D_T = A_v\nu\lambda^2\exp[(S_f^v + S_m^v)/k]\exp[-(E_f^v + E_m^v)/kT] \tag{11}$$

Here the response is characterized by the activation enthalpy $E_a = E_f^v + E_m^v$ expected for thermal vacancy self-diffusion. Thus, we expect the at-temperature irradiated diffusivity to merge with the thermal-only diffusivity at high temperature. This is the case here since an extrapolation of the thermal-only diffusivity in Fig. 7 to T > 1100 K will overlap with D′. The intermediate temperature range is dominated by the loss of point defects at sinks and the kinetic behavior becomes sink-limited. The effect of this kinetic regime, where the enhanced diffusivity ($D'_i + D'_v$) becomes temperature independent [2], is evident in Fig. 5 as a subtle plateau in D′ between 900 and 1000 K.

The best-fit of D' with Eq. (9) shown in Fig. 7 assumed $K = 0.024\text{ s}^{-1}$ (the calculated value for 1.8 MeV Kr^+ irradiation of CeO_2; for comparison we note that $K \sim 10^{-10}\text{ s}^{-1}$ for fast neutron irradiation), $\lambda = 0.382$ nm (the cation nearest-neighbor distance in CeO_2), $\nu \sim 10^{13}\text{ s}^{-1}$, and $\alpha \sim 10^{14}\text{ m}^{-2}$. This choice of α represents

an intermediate to high dislocation density typical of a lattice subjected to high displacement damage (dpa ~25 for the present work). The presence of dislocation defects was seen in Fig. 3 as broadening of the lattice mosaic under irradiation, especially at high temperature. The activation energies determined from the fit of D' are insensitive to the choice of α, however. The reason for this is simply that the enhanced diffusivity associated with sink-limited kinetics is independent of temperature and therefore not represented by an enthalpy. The values of D_o and E_a characterizing the Arrhenius response observed from D_T and D' at high temperature are listed in Table 2. The activation enthalpy ($E_m^v/2$) obtained from D' at low temperature is also listed in Table 2.

The consistency of the two sets of D_o and E_a values, determined independently from the at-temperature irradiation and the thermal-only data sets, indicates that thermal VSD on the cation sublattice in CeO_2 has been accurately characterized. The observation of recombination-limited kinetics RED over a sufficiently large temperature range below ~800 K allows us to effectively evaluate the vacancy migration enthalpy ($E_m^v = 2E_a \sim 0.4$ eV) as well. Given that $E_a = E_f^v + E_m^v \sim 1.4$ eV, we find $E_f^v \sim 1$ eV. Further analysis of the measured diffusivity behavior is presented in Fig. 7 inset. Here $\Delta D = D' - D_T$ (with D_T given by the parameters in the last row of Table 2) is plotted in an Arrhenius format and exhibits the kinetic behavior expected without the thermal VSD contribution [2]. Only the vacancy formation and migration energies were allowed to vary in the best-fit of ΔD; all other thermodynamic parameters were fixed to values obtained in the fit of D' with $K = 0.024\ s^{-1}$, $\lambda = 0.382$ nm, and $\alpha \sim 10^{14}\ m^{-2}$ as before. The best-fit of ΔD yielded $E_f^v \sim 0.9$ eV and $E_m^v \sim 0.5$ eV, consistent with the values obtained from the fit of D' and D_T in Fig. 7 and with $E_a = E_f^v + E_m^v \sim 1.4$ eV.

The diffusivities presented here were measured in a single crystal lattice and are not influenced by the presence of grain boundaries. Atomic coordination is reduced at grain boundaries and the presence of these interfaces can promote thermal diffusion, especially at lower temperatures, by acting as migration shortcuts with reduced activation enthalpy. Our measurement of D_T and D' therefore represents the true diffusivity on the cation sublattice in CeO_2. Most importantly, the use of a single crystal matrix eliminated the competing effect grain boundaries may have had on the observation of recombination-limited kinetics RED at low temperature and associated value E_m^v.

Generally, anion diffusion is orders of magnitude larger than metal cation diffusion in fluorite structures [14], is strongly influenced by oxygen stoichiometry [10], and is a function of dopant type and dopant concentration [14–16]. This rich and complex behavior is largely the effect of vacancies on the oxygen sublattice, the formation of defect (dopant–vacancy) clusters, and the interplay of electrostatic force and elastic strain [15]. The oxygen vacancy concentration is, in turn, controlled by T-pO_2 thermodynamic equilibrium, dopant valence, dopant concentration, and oxygen stoichiometry. The presence of a trivalent dopant, La for example, will induce vacancy formation on the oxygen sublattice via the neutrality condition $2La'_{Ce} = V_O^{\cdot\cdot}$. The requirement of local charge compensation leads to a dopant–vacancy defect cluster with an associated binding enthalpy. Oxygen vacancies bound to less mobile cation dopants are therefore not free to participate in oxygen diffusion and the temperature dependence of the dissociation of these defect clusters affects the observed oxygen migration enthalpy [15]. Given the myriad of influencing factors, it is not surprising the activation energy associated with anion diffusion in CeO_2 is known to vary from ~0.1 to ~3 eV [10,15,16].

We, of course, have not investigated anion diffusion, but rather cation diffusion. Low cation diffusivity in the fluorite structure is due to the high vacancy formation energy on the cation sublattice, which we have measured directly in CeO_2, and to the fact that cations are, in principle, excluded from the anion sublattice (and associated vacancy sites) by electrostatic forces. The use of a trivalent tracer (La) to measure diffusivity on the CeO_2 cation sublattice, for the reasons discussed above, can introduce convoluting effects in the evaluation of enthalpy. In particular, $La'_{Ce} - V_O^{\cdot\cdot}$ coupling may influence E_m^v on the cation sublattice, as it does on the anion sublattice. However, the migration enthalpy associated with the $V_O^{\cdot\cdot}$ defect will be small compared to the cation migration enthalpy and should not significantly affect diffusion on the cation sublattice. The presence of the La dopant may also influence the value of E_f^v we observed on the cation sublattice in CeO_2 since trivalent La is oversized compared to tetravalent Ce. However, the $V_O^{\cdot\cdot}$ defect will at least partially compensate the local dilatation associated with the oversized La dopant. The effect of the La dopant on E_f^v could be concentration dependent. The dopant concentration associated with a single La monolayer in CeO_2 is $\sim 10^{-2}$ when averaged over the entire 37 nm film thickness. This concentration is most appropriate at the highest temperatures investigated here where thermal VSD significantly broadens the La distribution. Dopant concentrations of order 10^{-2} to 10^{-1} are known to significantly influence anion diffusion in CeO_2 [10] and the same could hold for cation diffusion. These complicating factors may therefore limit the applicability of our data specifically to La diffusion on the cation sublattice in CeO_2. Unfortunately, we know of no other study characterizing cation diffusion in CeO_2 to compare.

In summary, thermal VSD and radiation-enhanced diffusion have both been characterized on the cation sublattice of single crystal CeO_2 using a lanthanum tracer layer. The results are unaffected by grain boundary interfaces and therefore represent true lattice diffusion. The observation of recombination-limited kinetics at low temperature permitted the direct measurement of the vacancy migration enthalpy ($E_m^v \sim 0.4$ eV). This evaluation, combined with the direct measurement of the vacancy activation energy from thermal VSD ($E_a \sim 1.4$ eV), allowed us to resolve the vacancy formation energy ($E_f^v \sim 1$ eV).

Acknowledgements

This work was performed with support from the US Department of Energy Nuclear Energy Research Initiative under Grant No. DEFG-07-14891. In addition, this work was carried out in part in the Frederick Seitz Materials Research Laboratory Central Facilities, University of Illinois, which are partially supported by the US Department of Energy under Grants DE-FG02-07ER46453 and DE-FG02-07ER46471. The film used in this study was grown by M. Zhang, a member of J. Eckstein's research group at the Univ. of Illinois, and this is gratefully acknowledged. The assistance of T. Spila (SIMS), D. Jeffers (ion accelerator), S. Burdin (profilometry), H. Ju (XRD), M. El-Bakhshwan (ion bombardment), X. Han (ion bombardment), and D. Heuser (data fitting) are all gratefully acknowledged. Finally, the authors are grateful to R. Averback for the use of the heated irradiation sample stage, for useful discussions regarding radiation-enhanced diffusivity, and for general interest in the work.

References

[1] R. Sizmann, J. Nucl. Mater. 69–70 (1978) 386.
[2] G.J. Dienes, A.C. Damask, J. Appl. Phys. 29 (1958) 1713.
[3] D.R. Olander, Fundamental Aspects of Nuclear Reactor Fuel Elements, National Technical Information Services, Springfield, VA, 1985.
[4] D. Olander, J. of Nucl. Mater. 389 (2009) 1.
[5] M. Saidy, W.H. Hocking, J.F. Mouris, P. Garcia, G. Carlot, B. Pasquet, J. Nucl. Mater. 372 (2008) 405.
[6] J.N. Eckstein, I. Bozovic, Annu. Rev., Mater. Sci. 25 (1995) 679.
[7] M. Zheng, Private Communication, 2010.
[8] M. Sunder, P.D. Moran, J. Electron. Mater. 38 (2009) 1931.

[9] N. Savvides, A. Thorley, S. Gnanarajan, A. Katsaros, Thin Solid Films 388 (2001) 177.
[10] A. Trovarelli (Ed.), Catalysis by Ceria and Related Materials, Imperial College Press, London, 2002.
[11] J.F. Ziegler, J.P. Biersack, V. Littmark, The Stopping and Range of Ions in Solids, vol. 1, Pergamon, New York, 1985.
[12] S.-J. Kim, M.-A. Nicolet, R.S. Averback, D. Peak, Phys. Rev. B 37 (1988) 38.
[13] A.I. Van Sambeek, R.S. Averback, C.P. Flynn, M.H. Yang, W. Jager, J. Appl. Phys. 83 (1998) 7576.
[14] T.H. Etsell, S.N. Flengas, Chem. Rev. 70 (1970) 339.
[15] J.A. Kilner, Solid State Ionics 129 (2000) 13.
[16] O.T. Sorensen (Ed.), Nonstoichiometric Oxides, Academic Press, New York, 1981.